Supplementary Information for:

Epoxide-driven secondary organic aerosol formation is modulated by aerosol-cloud cycling

Payton Beeler[1], Alla Zelenyuk[1], Manish Shrivastava[1], Koichi Sakaguchi[1], Jerome D. Fast[1], David M. Bell[2], Siegfried Schobesberger[3], John Shilling[1], Joel Thornton[4], and Laura Fierce[1*].

[1]Atmospheric, Climate, and Earth Sciences Division, Pacific Northwest National Laboratory, Richland, WA, 99354, USA
[2]Laboratory of Atmospheric Chemistry, Paul Scherrer Institute, Villigen 5232, Switzerland
[3]Department of Technical Physics, University of Eastern Finland, 70210 Kuopio, Finland
[4]Department of Atmospheric Sciences, University of Washington, Seattle, WA, 98195, USA

[*]*Correspondence to*: Laura Fierce (laura.fierce@pnnl.gov)

Section S1: WRF-LES Configuration

The model configuration follows Fast et al. (2019)[36] and is briefly summarized here. We use one-way nested domains from the 300-m grid spacing in the outer domain to the 100-m grid in the inner domain. In both domains, the vertical grid spacing is 24 m in the lower atmosphere, gradually coarsened above ~ 6.2 km to the top of the domain at 16. 2 km above the mean sea level. The outer domain size is 300 x 300 km, and the inner domain covers a 120 x 120 km area centered at the ARM SGP central facility (see Figure S10). We use the following physics parameterizations: the RRTMG shortwave and longwave radiation[37], the Thompson microphysics[38], the revised MM5 Monin-Obukhov surface layer[39], the turbulent kinetic energy closure for sub-grid turbulence[40], and the Noah land surface model[41].

The WRF model is integrated from 12:00 UTC (6:00 CST) to 23:00 UTC (17:00 CST) on April 25, 2016. The three-dimensional output from the inner domain is written at a one-minute frequency. The atmospheric initial and boundary conditions are obtained from the European Centre for Medium-Range Weather Forecasts (ECMWF) High-Resolution operational analysis with a nominal grid spacing of 9 km[42]. Recently developed land-data assimilation data with 1-km grid spacing is used for the initial soil moisture and temperature[43]. Compared to the ARM SGP Central Facility sounding, the ECMWF analysis well captured the early-morning temperature, humidity, and wind directions in the lowest ~1.5 km of the atmosphere. However, the wind speed is ~ 5 m/s too low between 1 and 1.5 km AGL, and the sharpness of the inversion around 1.5 km above the surface is also underestimated (Figure S11) which could affect boundary-layer growth during the model integration. Consistent with this initial condition, the simulated near-surface specific humidity and wind directions agree well with the surface observations throughout the integration, but the 10-m wind speed is underestimated by 1-2 m/s (Figures S11-12). Also, the simulated 2-m air temperature is higher than observed by ~ 2 °C (Figure S10d), which may be caused by overestimated sensible heat flux in the morning (Figure S12e). Still, the WRF-LES reproduce cloud development seen in the GOES retrieval (Figure S13).

Section S2: Background trace gas concentrations from aircraft measurements

The background concentration of sulfate, nitrate, and IEPOX SOA precursors are approximated as a function of altitude and are informed by chemical ionization mass spectrometry (CIMS)

measurements on board the G-1 aircraft[44]. CIMS measurements are averaged over G-1 flight legs that intersect air parcels, resulting in vertical concentration profiles for each chemical species. We assume that the background concentration of trace gases follows the CIMS measurements and are interpolated as a function of the altitude of the air parcel. When air parcels are outside the limits of CIMS measurements, exponential approximations are used to extrapolate the trace gas concentrations (see Figure S14). For trace gases that were not measured by CIMS, we use vertical concentration profiles from a standard atmosphere model[45].

Section S3: Droplet activation in LD-Chem model

Water uptake on particles in each particle-resolved simulation is based on previously published models[27,46]. The rate of change in droplet radius is given by

$$\frac{dr_i}{dt} = \frac{G}{r_i}\left(s - s_{eq,i}\right), \tag{2}$$

where r_i is the radius of particle i, s is the supersaturation, $s_{eq,i}$is the equilibrium supersaturation of droplet i, and G is the droplet growth coefficient, given by

$$G = \left\{\frac{\rho_w RT}{e_s D_v' M_w} + \frac{L\rho_w[(LM_w/RT)-1]}{k_a' T}\right\}^{-1}. \tag{3}$$

Here, ρ_w is the density of water, R is the universal gas constant, T is the temperature, e_s is the saturation vapor pressure, M_w is the molar mass of water, L is the latent heat of vaporization of water, D_v' is the diffusivity of air, and k_a' is the thermal conductivity of air. To account for non-continuum effects on the diffusivity and of air, D_v' is calculated using

$$D_v' = \frac{D_v}{1+\frac{D_v}{\alpha_c r_i}\sqrt{\frac{2\pi M_w}{RT}}}, \tag{4}$$

where ρ_a is the density of air, D_v is the diffusivity of air, and α_c is the condensation coefficient. We also account for non-continuum effects on the thermal conductivity of air, and calculate k_a' using

$$k_a' = \frac{k_a}{1+\frac{k_a}{\alpha_T r_i \rho_a c_p}\sqrt{\frac{2\pi M_a}{RT}}}, \tag{5}$$

where k_a is the thermal conductivity of air, α_T is the thermal accommodation coefficient, and M_a is the molar mass of dry air. The droplet equilibrium supersaturation is calculated using κ-Köhler theory, and is related to the hygroscopicity parameter (κ) by

$$s_{eq,i} = a_w \exp\left[\frac{2\sigma_w M_w}{RT\rho_w r_i}\right], \tag{6}$$

where σ_w is the surface tension of water, and

$$a_w = \left[1 + \frac{1}{V_{tot}}\left(\sum_{j=1}^{N_j} V_j \kappa_j\right)\left(\frac{r_d^3}{r}\right)\right]^{-1}. \tag{7}$$

Here, V_{tot} is the total volume of the dry particle, V_j is the volume of species j in the droplet, κ_j is

the hygroscopicity parameter of species j, r_d is the dry radius, and N_j is the number of dry species present in the droplet. Values for all constants used in Equations 1-6 can be found in supplementary Table S4.

Section S4: Optimization Procedure for Initial Aerosol Populations

Initialization of aerosol populations in particle-resolved simulations begins by randomly distributing each class of particle (sulfate rich, nitrate rich, organic, dust, black carbon, and IEPOX SOA rich) amongst the modes of the measured size distribution, while enforcing that the fraction of particles larger than 85 nm must match the miniSPLAT-measured value[15,47]. We then used combined squared normalized residual (RSS) to quantify how closely the number concentration, surface area concentration, and mass fraction of each chemical species matches measurements. This process is repeated 1,000 times and the model configuration which minimizes RSS is used to initialize the size distribution of each particle class. It should be noted that we assume separate size distributions for black carbon (BC) and dust particles, with lognormal distributions given by previous publications[48].

Once the size distribution of each particle class has been determined, the mass of each chemical species in each particle is determined. The chemical composition of a particle in class A is determined by firstly generating a random number following a Gaussian probability distribution with a given average (μ) and standard deviation of 0.1. The generated random number (x) must be greater than a user-defined minimum mass fraction of A within each particle of type A (β). If x is greater than β, then the mass fraction of A in the particle will be equal to x, and the rest of the particle's mass is made up of other randomly selected species. Detailed knowledge of β for each particle class would require rigorous analysis of the mass spectra of each individual particle, detailed chamber experiments for each compound of interest (both infeasible for time purposes), or the ability to map between mass spectra and mass fraction (a longstanding challenge for mass spectrometry techniques). Detailed analysis of miniSPLAT mass spectra from chamber experiments show that IEPOX SOA rich particles are at least 30% IEPOX SOA by mass[35]. Based on this we assume that β is 0.3 for IEPOX SOA particles, and that β is 0.5 for all other particle classes. All particles are neutralized during the model initialization by balancing the mole fractions of sulfate and nitrate with ammonium.

The initialization procedure outlined here generates a particle population that represents the particle-scale compositional diversity measured by miniSPLAT, while preserving bulk chemical composition and size distribution information. We initialize each air parcel with 100 computational particles and use a 5 second time step to best balance statistical accuracy and computational costs (see Figures S5-6). An overview of the initialization procedure can be found in Figure S15, and the initial size distribution and bulk composition of each particle-containing air parcel is shown in Figure S16.

Table S1. Gas-phase photolysis and thermal reactions included in particle-resolved simulations. Unless otherwise noted, all reactions and rate constants are taken from McNeill et. al. 2012 and have the form $k(T) = k_0 \exp(-E_a/RT)$.

Reaction	k_0 ((mol/m^3)$^{n-1}$/s)	$-E_a/R$ (K)	Notes
$H_2O_2 + h\nu \rightarrow 2OH$	7.66×10^{-6}		
$O_3 + h\nu \rightarrow O(^1D) + O_2$	3.55×10^{-5}		
$O_3 + h\nu \rightarrow O(^3P) + O_2$	2.08×10^{-4}		
$NO_2 + h\nu \rightarrow NO + O(^3P)$	8.79×10^{-3}		
$NO_3 + h\nu \rightarrow NO_2 + O(^3P)$	1.53×10^{-1}		
$NO_3 + h\nu \rightarrow NO + O_2$	2.21×10^{-2}		
$HNO_3 + h\nu \rightarrow NO_2 + OH$	6.56×10^{-7}		
$HONO + h\nu \rightarrow NO + OH$	1.95×10^{-3}		
$N_2O_5 + h\nu \rightarrow NO_2 + NO_3$	2.54×10^{-5}		
$O(^1D) + N_2 \rightarrow O(^3P) + N_2$	1.08×10^{7}	100	
$O(^1D) + O_2 \rightarrow O(^3P) + O_2$	1.93×10^{7}	70	
$O(^3P) + O_2 + M \rightarrow O_3$	2.18×10^{2}	690	
$O(^1D) + H_2O \rightarrow 2OH$	1.32×10^{2}		
$O_3 + OH \rightarrow HO_2 + O_2$	9.64×10^{5}	–940	
$O_3 + HO_2 \rightarrow OH + 2O_2$	6.62×10^{3}	–500	
$NO + OH + M \rightarrow HONO$	2.76×10^{24}		
$O_3 + NO \rightarrow NO_2 + O_2$	1.20×10^{6}	–1400	
$O_3 + NO_2 \rightarrow NO_3 + O_2$	7.23×10^{4}	–2450	
$NO + NO_3 \rightarrow 2NO_2$	9.03×10^{6}	170	
$NO_2 + NO_3 + M \rightarrow N_2O_5$	4.71×10^{23}		
$N_2O_5 + M \rightarrow NO_2 + NO_3$	4.09×10^{16}	–11080	
$NO_2 + OH + M \rightarrow HNO_3$	3.52×10^{24}		
$NO_2 + HO_2 + M \rightarrow HNO_4$	5.44×10^{23}		
$HNO_4 + M \rightarrow NO_2 + HO_2$	4.64×10^{6}	–10420	
$CO + OH \rightarrow CO_2 + HO_2$	9.03×10^{4}		
$2HO_2 + M \rightarrow H_2O_2 + O_2$			[1]
$H_2O_2 + OH \rightarrow HO_2 + H_2O$	1.75×10^{6}	–160	
$HO_2 + NO \rightarrow NO_2 + OH$	2.11×10^{6}	250	
$HO_2 + OH \rightarrow H_2O + O_2$	2.89×10^{7}	250	
$SO_2 + OH + M \rightarrow HOSO_2$			[2]
$HOSO_2 + O_2 \rightarrow HO_2 + SO_3$	7.83×10^{5}	–330	[3]
$SO_3 + 2H_2O \rightarrow H_2SO_4$	1.41×10^{-5}	6830	[3]
$ISOP + OH + O_2 \rightarrow ISOPOO$	1.26×10^{7}	465	[3]
$ISOPOO + HO_2 \rightarrow ISOPOOH + O_2$	1.02×10^{7}		[3]
$ISOPOOH + OH \rightarrow IEPOX + OH$	1.14×10^{7}	390	

[1] Third-body reactions with O_2 and N_2, rate constant[49] is given by $k(T) = [1.32 \times 10^5 \exp(600/T) + 6.9 \times 10^2 [N_2] \exp(980/T)] \times [1.0 + 8.4 \times 10^{-4} [H_2O] \exp(2200/T)]$. Data Sheet HOx14.

[2] Rate coefficient is calculated according to IUPAC preferred low-pressure and high-pressure limits with Troe falloff kinetics[50]. Data Sheet SOx15.

[3] Values taken from IUPAC recommendations[51]: data sheets SOx16, SOx47, HOx_VOC8, and HOx_VOC81.

Table S2. Names and Henry's Law constants for water-soluble gases included in particle-resolved model. Temperature dependent Henry's Law constant is given by $H(T) = H_0 \exp[-\Delta H_{sol}/R(1/T - 1/T_0)]$, where T_0 is 298 K. All values are taken from Leriche et. al. 2003, unless otherwise noted.

Gas	α	H_0 (M/atm)	$-\Delta H_{sol}/R$ (K)	Notes
SO_2	0.11	1.4×10^{0}	2900	
O_3	0.05	1.1×10^{-2}	2300	
H_2SO_4	0.07	2.1×10^{5}	8700	
IEPOX	0.001	2.0×10^{6}	4400	[1]
H_2O_2	0.11	8.33×10^{4}	7400	
NO_2	0.0015	1.2×10^{-2}	1260	
HNO_2	0.05	5.0×10^{1}	4900	
HNO_3	0.054	2.1×10^{5}	8700	
HNO_4	0.05	1.2×10^{4}	6900	
NH_3	0.04	6.1×10^{1}	3920	
OH	0.05	3.0×10^{1}	4500	
HONO	0.05	5.0×10^{1}	4900	
N_2O_5	0.0037	2.1×10^{0}	3400	
CO_2	0.0002	3.6×10^{-2}	2200	
ISOP	0.028	1.0×10^{-4}		[2]

[1] Values taken from Zhang et. al. 2023[9].

[2] Value taken from McNeill et. al. 2012[26].

Table S3. Aqueous-phase reactions included in particle-resolved simulations. Temperature dependent rate constants are given by $k(T) = k_0 \exp[-E_a/R(1/T - 1/T_0)]$, where T_0 is 298 K. Unless otherwise noted, all reaction rate constants are taken from Seinfeld and Pandis (2016).

Reaction	k_0 ((mol/m^3)$^{n-1}$/s)	$-E_a/R$ (K)	Notes
$SO_2 \rightarrow HSO_3^- + H^+$	5.0×10^5	1960	
$HSO_3^- + H^+ \rightarrow SO_2$	3.85×10^4	1960	
$HSO_3^- \rightarrow SO_3^{2-} + H^+$	5.0×10^5	1500	
$SO_3^{2-} + H^+ \rightarrow HSO_3^-$	7.5×10^9	1500	
$H_2SO_4 \rightarrow HSO_4^- + H^+$	5.0×10^5		
$HSO_4^- + H^+ \rightarrow H_2SO_4$	5.0×10^2		
$HSO_4^- \rightarrow SO_4^{2-} + H^+$	5.0×10^3	2720	
$SO_4^{2-} + H^+ \rightarrow HSO_4^-$	5.0×10^5	2720	
$S(IV) + O_3 \rightarrow S(VI)$	$k_{O3,1} + k_{O3,2} + k_{O3,3}$		[1,2]
$S(IV) + H_2O_2 \rightarrow S(VI)$	$k_{HP,1}/(1+k_{HP,2})$		[1,3]
$S(IV) + NO_2 \rightarrow S(VI) + NO$	1.24×10^4		[1]
$S(IV) + HNO_2 \rightarrow S(VI)$	2.0×10^6		[1]
$S(IV) + O_2 \rightarrow S(VI)$	$k_{O2,1}$		[1,4]
$IEPOX + H_2O + H^+ \rightarrow tetrol + H^+$	1.0×10^{-8}		
$IEPOX + HSO_4^- \rightarrow IEPOX\ OS$	1.46×10^{-7}		
$IEPOX + SO_4^{2-} + H^+ \rightarrow IEPOX\ OS + H^+$	1.06×10^{-8}		
IEPOX + tetrol $\rightarrow$ tetrol oligomers	3.54×10^{-2}		
$H_2O_2 + h\nu \rightarrow 2\ \cdot OH$	2.8×10^{-6}		[5]
$\cdot OH + \cdot OH \rightarrow H_2O_2$	3.6×10^6		[5]
$\cdot OH + H_2O_2 \rightarrow H_2O + HO_2$	2.7×10^4	1700	[5]
$\cdot OH + HO_2 \rightarrow H_2O + O_2$	6.0×10^6		[5]
$\cdot OH + O_2^- \rightarrow OH + O_2$	3.5×10^7	720	[5]
$HO_2 \rightarrow O_2^- + H^+$	8.0×10^3		[5]
$O_2^- + H^+ \rightarrow HO_2$	5.0×10^5		[5]
$IEPOX + \cdot OH \rightarrow IEPOX\ SOA$			[5]
$NH_3 \rightarrow NH_4^+ + OH^-$	8.5×10^0	-450	
$NH_4^+ + OH^- \rightarrow NH_3$	5.0×10^5	-450	
$2NO_2 \rightarrow NO_3^- + H^+$	1.0×10^5	1500	
$NO + NO_2 \rightarrow 2NO_2^- + 2H^+$	2.0×10^5	1500	
$NO_2 + \cdot OH \rightarrow NO_3^- + H^+$	1.2×10^7		
$NO_2^- + O_3 \rightarrow NO_3^- + O_2$	5.0×10^3	6950	
$HNO_3 \rightarrow NO_3^- + H^+$	5.0×10^5	8700	
$NO_3^- + H^+ \rightarrow HNO_3$	3.2×10^4	8700	

[1] Values are taken from Liu et. al. 2021[3]

[2] $k_{O3,1} = 4.9\times10^1[SO_2]$, $k_{O3,2} = 6.2\times10^2[HSO_3^-]\exp[-5530(1/T - 1/T_0)]$, and $k_{O3,3} = 4.0\times10^6[SO_3^{2-}]\exp[-5280(1/T - 1/T_0)]$, where all concentration units are in mol/m^3.

[3] $k_{HP,1} = 1.5\times10^2[HSO_3^-][H^+]\exp[-4430(1/T - 1/T_0)]$, $k_{HP,2} = 1.3\times10^{-2}[H^+]$

[4] $k_{O2,1} = 8.72\times10^7[H^+]^{-0.74}[Mn(II)][Fe(III)]$ for pH ≤ 4.2 and $k_{O2,1} = 7.51\times10^{13}[H+]^{0.67}[Mn(II)][Fe(III)]$ for pH > 4.2. Transition metal ion concentrations are calculated as a function of pH according to Seinfeld and Padis 2016[25].

[5] Mechanism is based on Otto et. al. 2019[52].

Table S4. Constants used to calculate water uptake. All values are based on Rothenberg and Wang 2016[27].

Constant	Abbreviation	Value	Units
Gravitational constant	g	9.8	m/s^2
Specific heat of dry air	C_p	1004.0	
Density of water	ρ_w	1000.0	kg/m^3
Gas constant for dry air	R_d	287.0	
Gas constant for water vapor	R_v	461.5	
Gas constant	R	8.314	m^3 Pa/mol K
Molecular weight of water	M_w	0.018	kg/mol
Molecular weight of dry air	M_a	0.0289	kg/mol
Diffusivity of water vapor in air	D_v	3.0×10^{-5}	m^2/s
Latent heat of vaporization of water	L_v	2.25×10^6	
Condensation coefficient	α_c	1.0	
Thermal conductivity of air	k_a	0.02	
Thermal accommodation coefficient	α_T	0.96	
Boltzmann constant	k_b	1.38×10^{-23}	

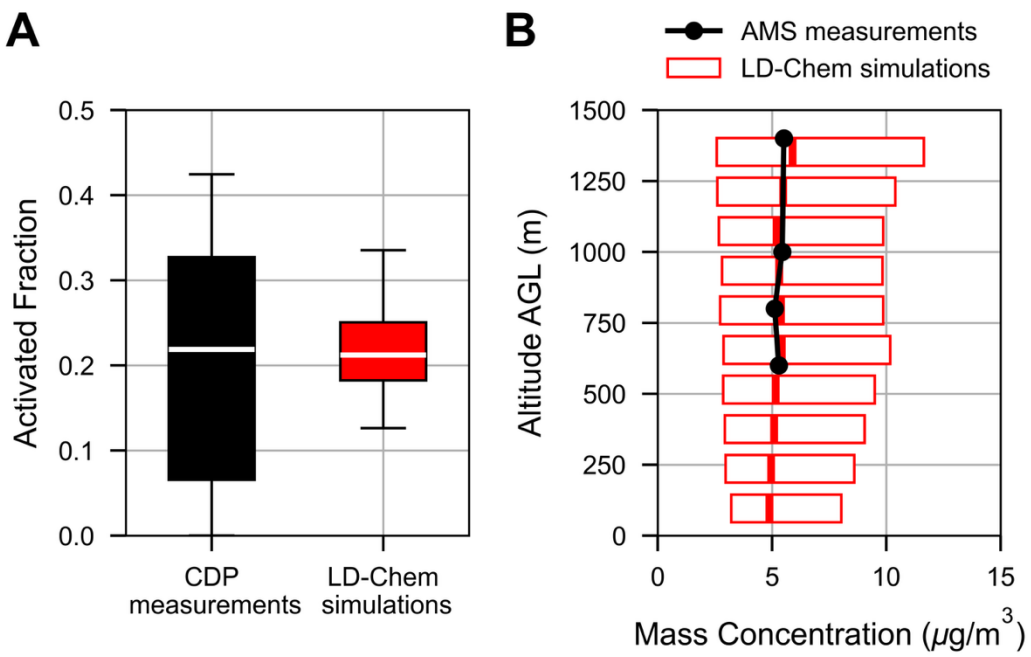

134

135 **Figure S1.** The fraction of particles that activate into cloud droplets in LD-Chem simulations agrees well with CDP
136 measurements **(A)**. Simulations also predict that the mass mixing ratio increases from 5.4 μg/m^3 at an altitude of 600
137 m to 5.9 μg/m^3 at an altitude of 1300 m, which is also in good agreement AMS measurements **(B)**.

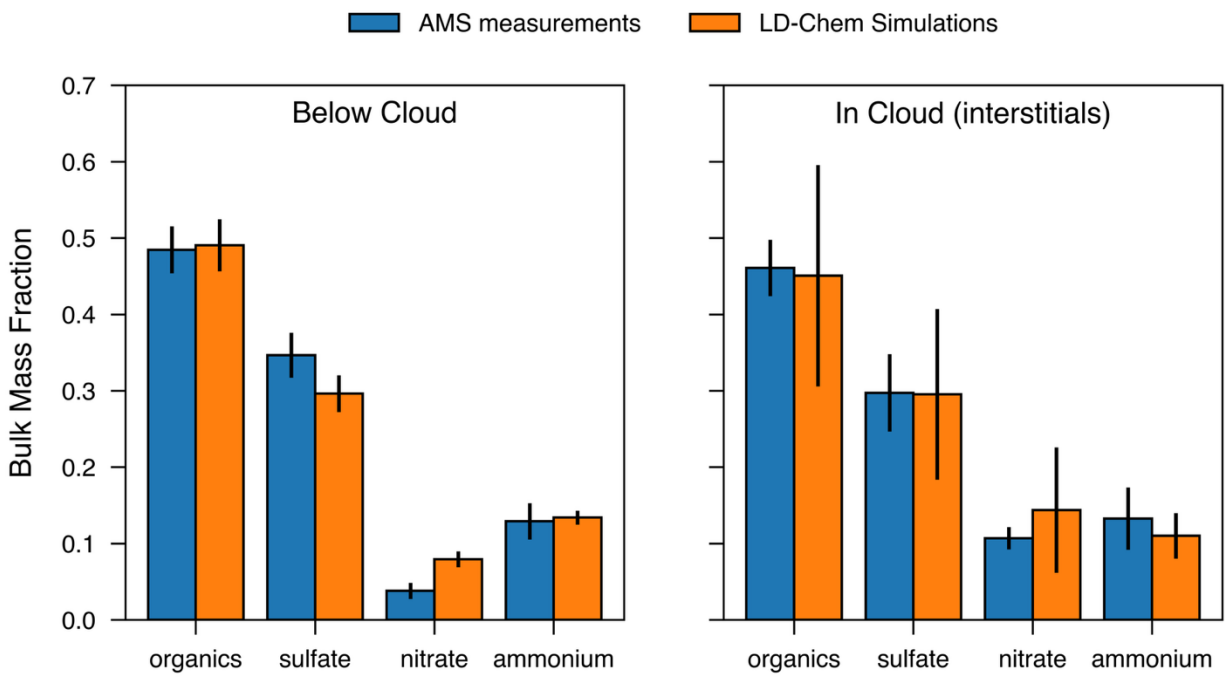

138

139 **Figure S2.** Bulk mass fraction of individual species in LD-chem simulations agrees well with AMS measurements
140 below the cloud layer (left) and in the cloud layer (right) on April 25th. It should be noted that we do not include cloud
141 droplet residuals in the right panel to avoid possible compositional changes as particles are dried before measurement
142 by the AMS.

143

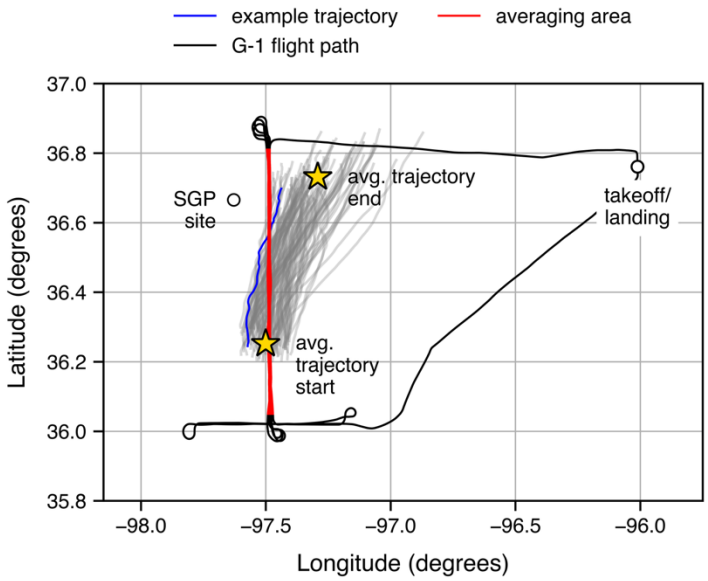

144

145 **Figure S3.** Flight path of G-1 aircraft on April 25th. We used measurements from six north-south transects of the G-1
146 flight for comparison with Lagrangian Droplet (LD) simulations (averaging area). Measurements of trace gas
147 concentrations on these flight legs were also used to inform vertically resolved trace gas concentrations in LD
148 simulations.

149

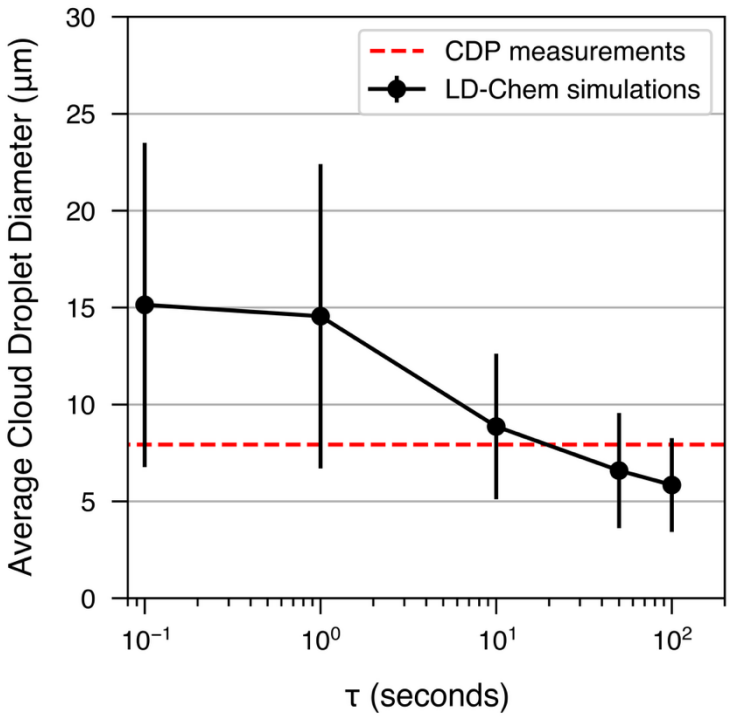

Figure S4. Average cloud droplet diameter as a function of mass transfer timescale between background and air parcels (τ) in 10 LD-Chem simulations . Setting τ = 24.5 s reconciles the simulated average cloud droplet diameter with cloud droplet probe (CDP) measurements and is therefore used in all simulations.

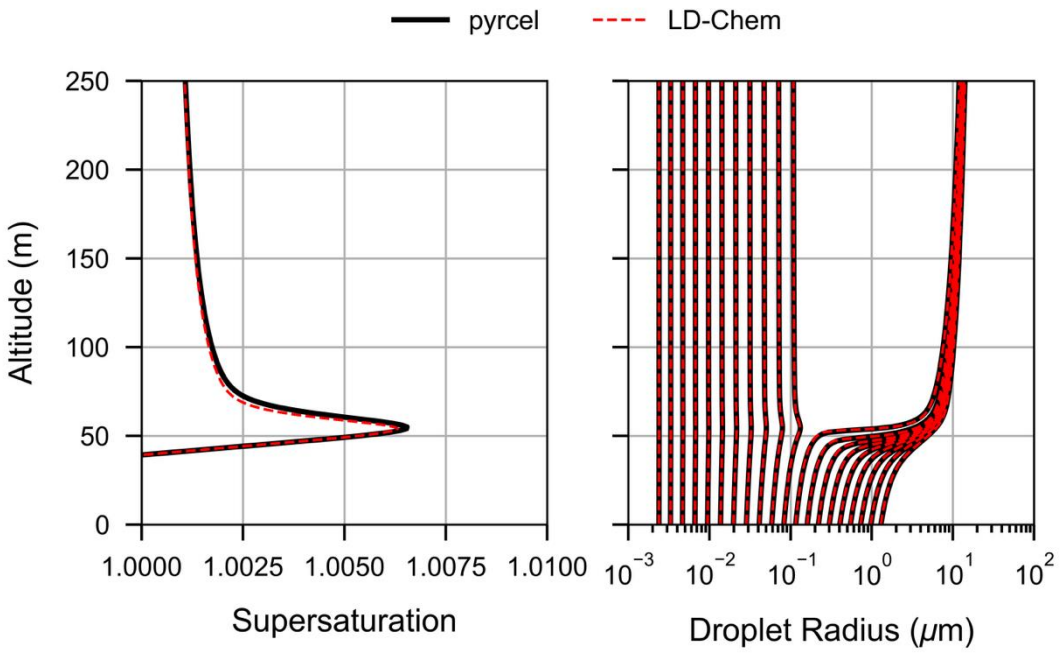

Figure S5. Comparison of full-coupled parcel model simulations (pyrcel) and process-split LD-Chem simulations. We find that droplet activation and subsequent supersaturation adjustments are accurately captured in LD-Chem simulations.

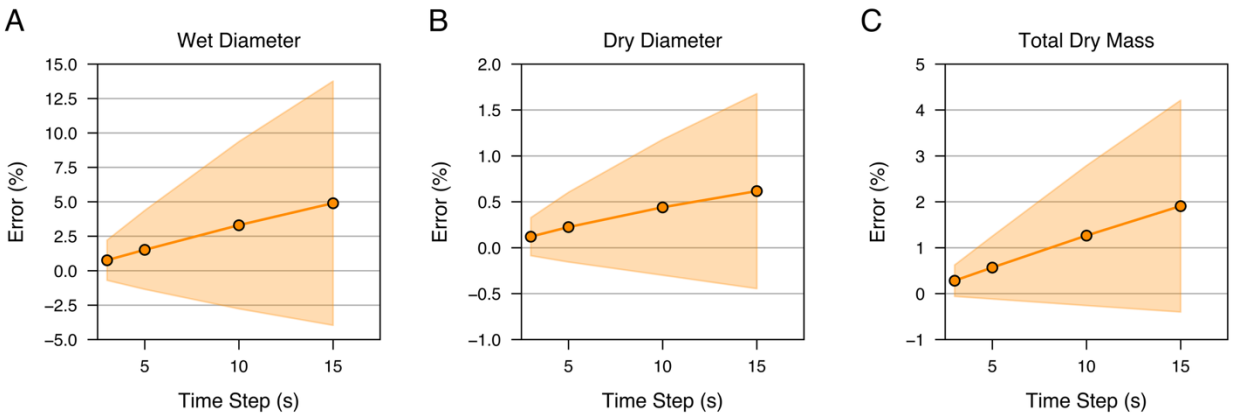

Figure S6. Effects of simulation time step on final wet diameter **(A)**, dry diameter **(B)**, and dry mass **(C)** in 10 process-split LD-Chem simulations. Points represent average error and shaded areas represent one standard deviation. Here, error is calculated compared to simulations with identical initial conditions and a 1.0 second time step. Maintaining a time step of 5 seconds or less introduces less than 5% error for all values and is therefore used in this work.

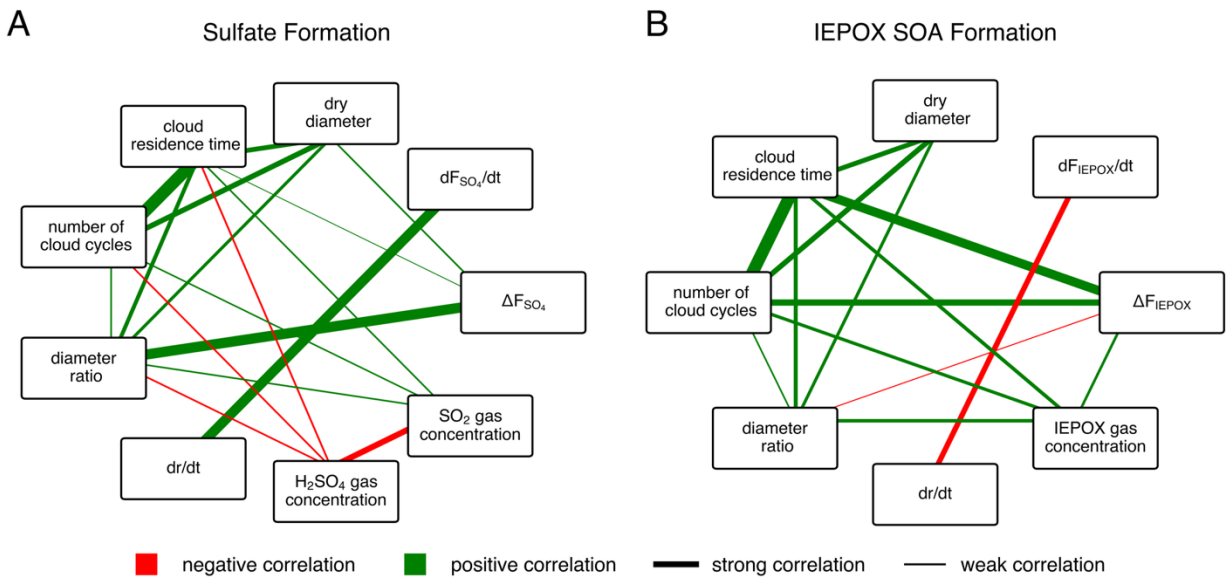

Figure S7. Correlation network diagram of variables associated with sulfate formation **(A)** and IEPOX SOA formation **(B)**. The rate of change in per-particle sulfate mass fraction (dF_{SO4}/dt) has a strong positive correlation with the rate of change in particle radius (dr/dt). The total change in per-particle sulfate mass fraction (ΔF_{SO4}) also has a strong positive correlation with the diameter ratio. These correlations show that sulfate formation is dominated by in-cloud oxidation of SO_2 and not by dissolution of H_2SO_4 in humidified aerosols. However, the rate of change in per-particle IEPOX SOA mass fraction (dF_{IEPOX}/dt) is negatively correlated with dr/dt, indicating that IEPOX SOA formation is occurring as cloud droplets evaporate. Additionally, strong positive correlation between IEPOX SOA and number of cloud cycles shows that multiple rounds of activation-evaporation lead to higher changes in per-particle IEPOX SOA mass fraction.

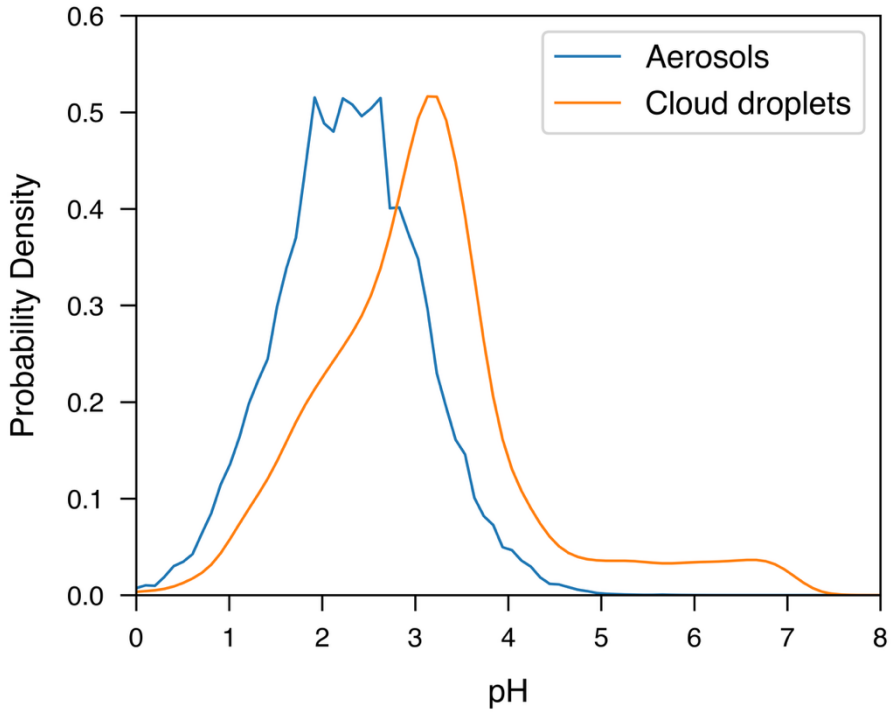

Figure S8: Distribution of pH of aerosol particles and cloud droplets. The pH of aerosols agrees well with measured pH during the Spring intensive observation period[34] and cloud droplet pH is in line with estimates from global models[53] and cloud chamber simulations[12].

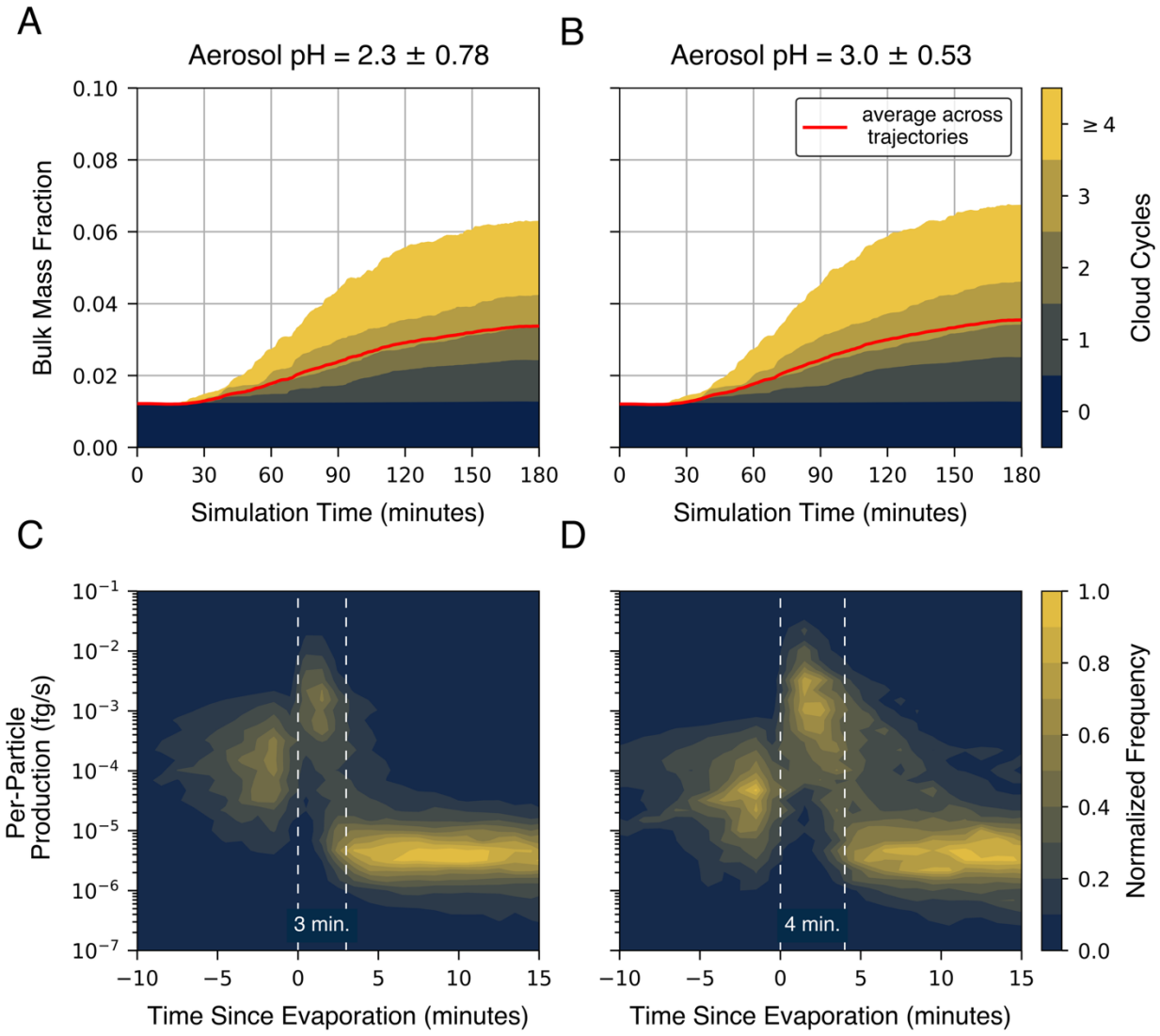

Figure S9: Sensitivity tests showed that the simulated bulk IEPOX mass fraction was not sensitive to aerosol pH **(A-B)**. However, increasing the aerosol pH from 2.3 to 3.0 led to an 18% increase in the total IEPOX SOA mass concentration. Increasing aerosol pH slightly lengthened the window of time when IEPOX SOA formation spikes after droplet evaporation from 3 to 4 minutes **(C-D)**, but does not significantly affect overall IEPOX SOA production, leading to the observed increase in IEPOX SOA mass concentrations.

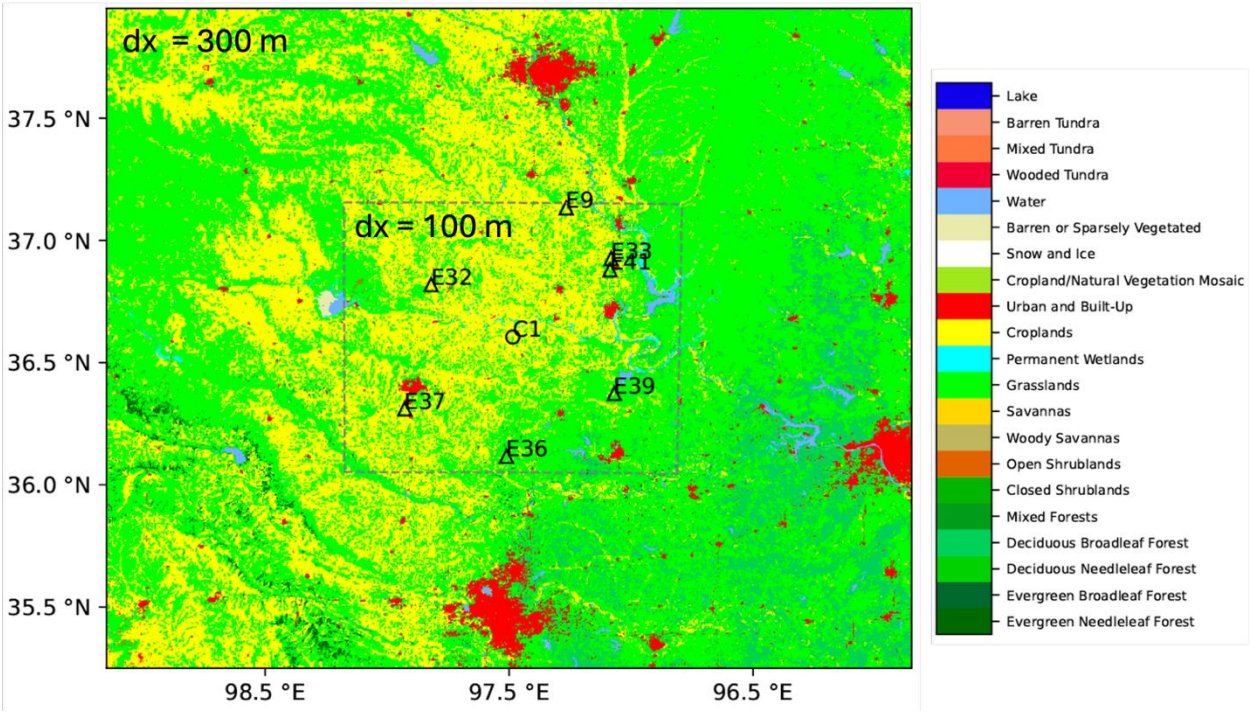

Figure S10. Outer (300 m) and inner (100 m) domain of WRF-LES simulations. Color represents the land cover type within the simulations. Point C1 represents the ARM Southern Great Plains site and triangular points are used to evaluate the wind speed, wind direction, temperature, and moisture in WRF-LES against observations.

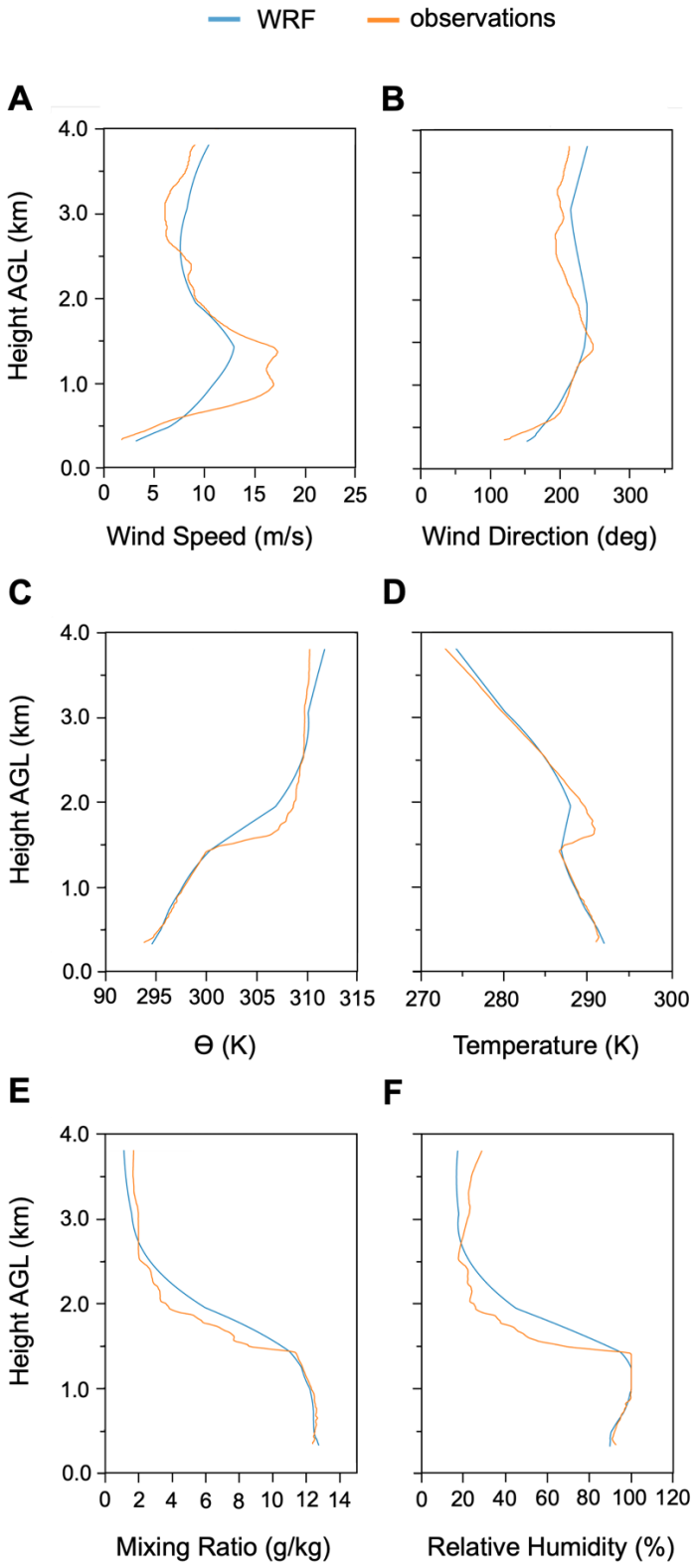

Figure S11. Comparison of WRF-LES initial wind speed at 12:00 UTC **(A)**, wind direction **(B)**, potential temperature **(C)**, temperature **(D)**, water vapor mixing ratio **(E)**, and relative humidity **(F)** compared with observations from the ARM SGP site.

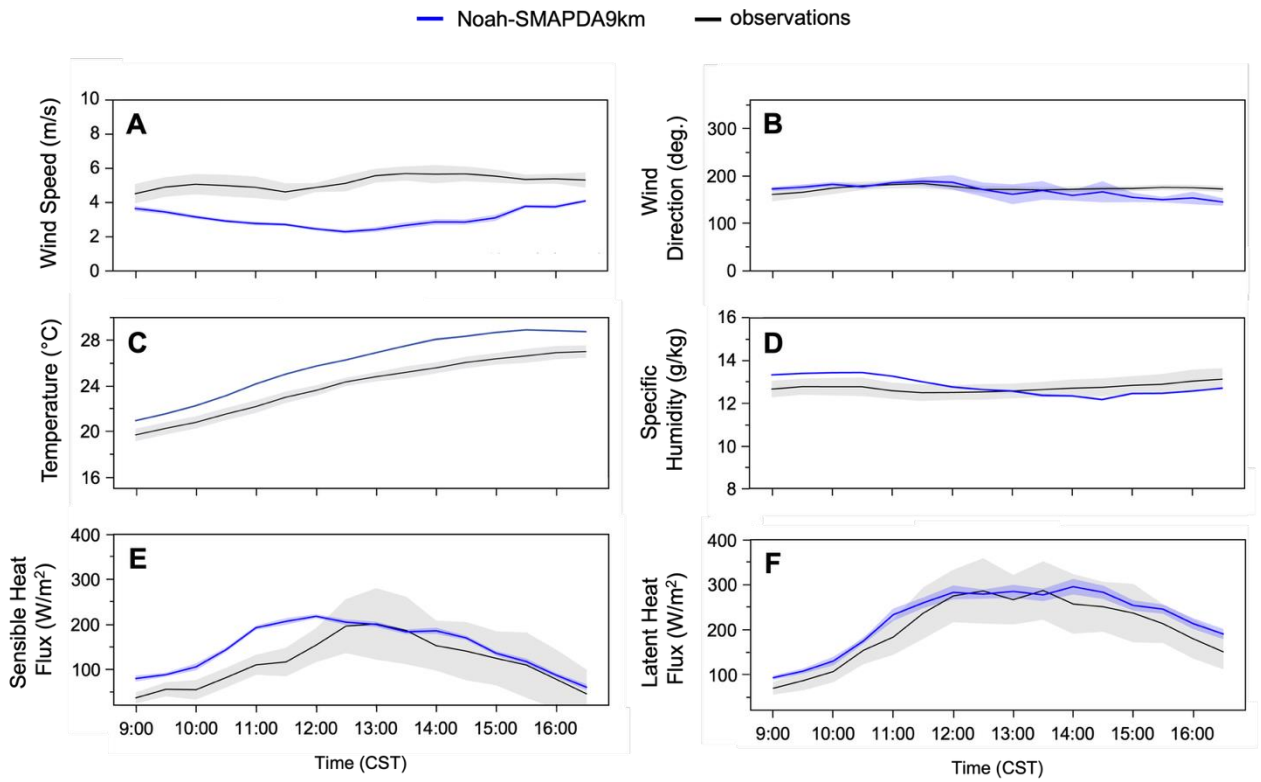

Figure S12. 10-m WRF-LES wind speed **(A)** and wind direction **(B)**, 2-m temperature **(C)**, 2-m humidity **(D)**, sensible heat flux **(E)**, and latent heat flux **(F)** throughout model integration compared with observations averaged across SGP observational sites (triangular points in Figure S8).

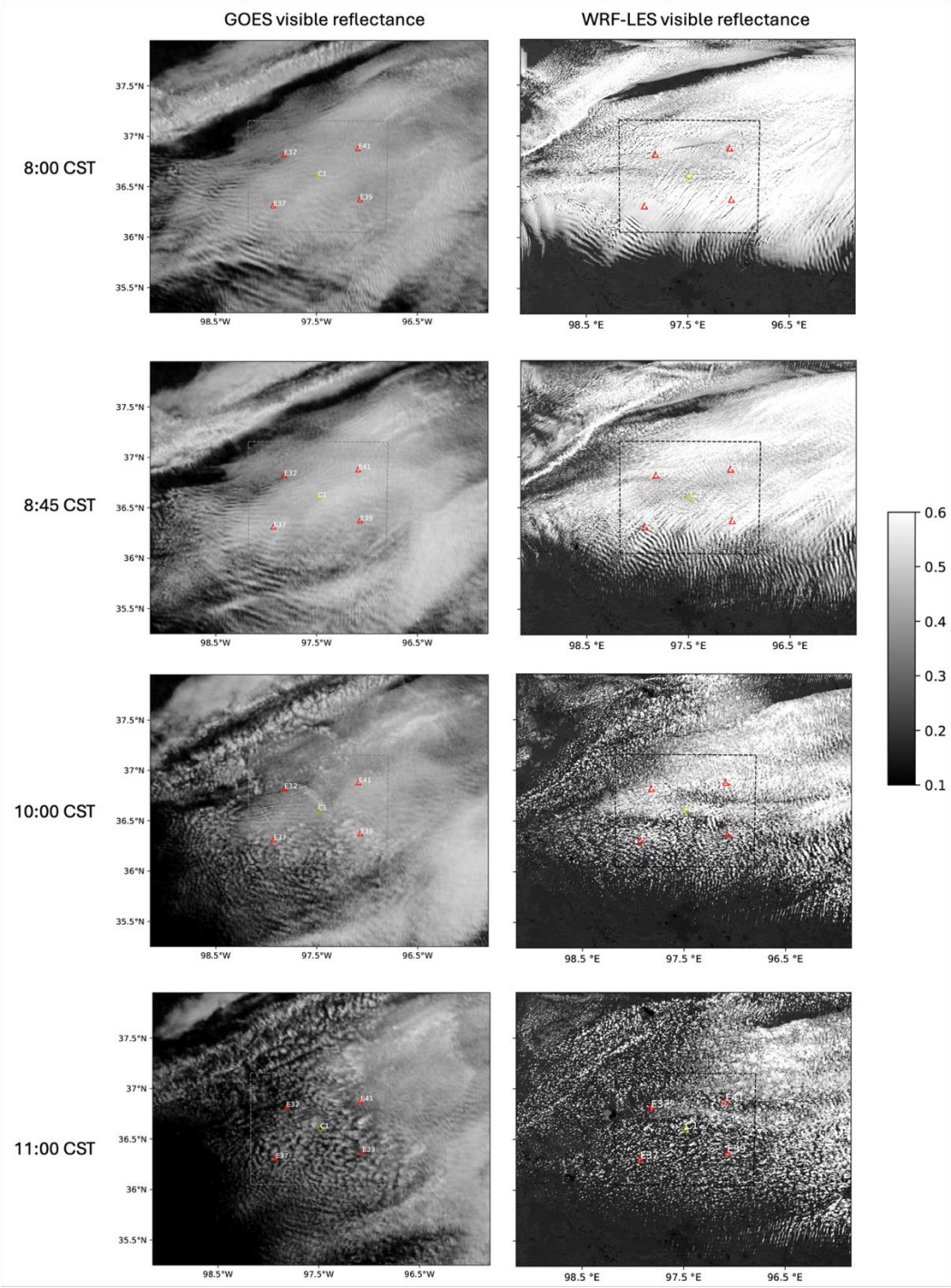

205

206 **Figure S13.** WRF-LES visible reflectance (right column) compared with observations from GOES satellite (left
207 column) during model integration shows that cloud development is well captured in the model domain. The five
208 marked sites represent ARM vertical profiling sites. Aircraft sampling is performed within this region.

209

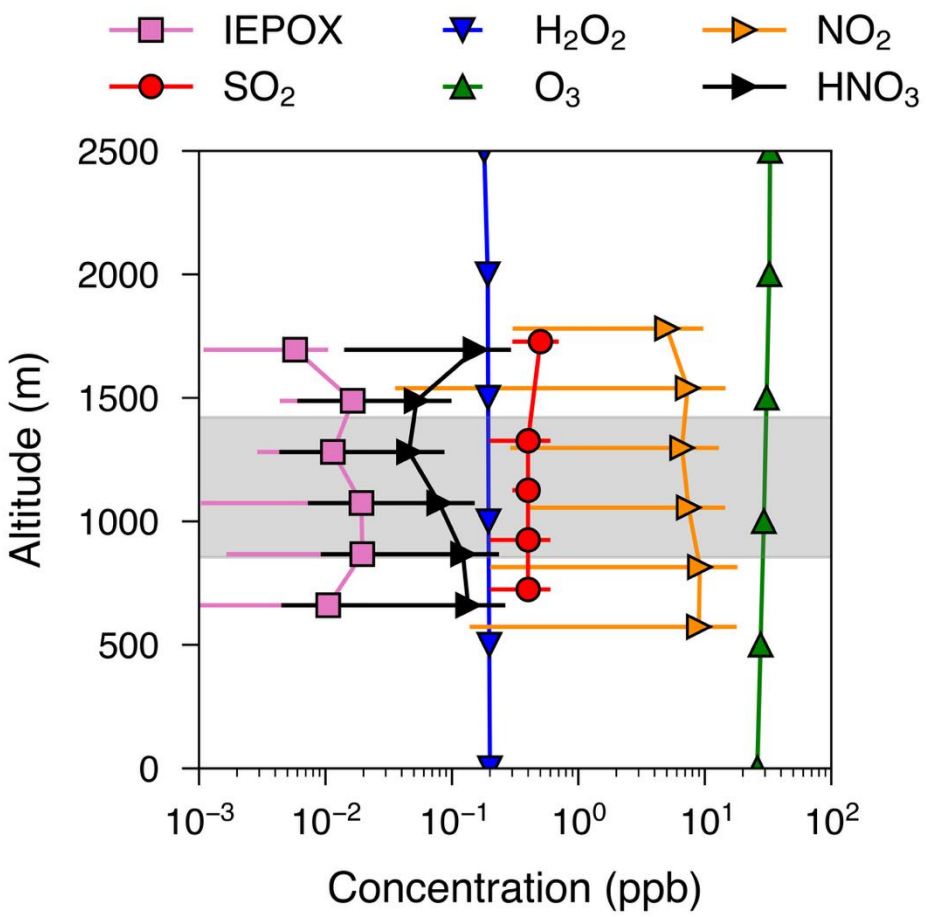

Figure S14. Background trace gas concentrations as a function of altitude in LD-Chem simulations. the background concentration of trace gases was interpolated as a function of the altitude of the air parcel at each time step. When air parcels are outside the limits of available data, exponential approximations are used to extrapolate the trace gas concentrations.

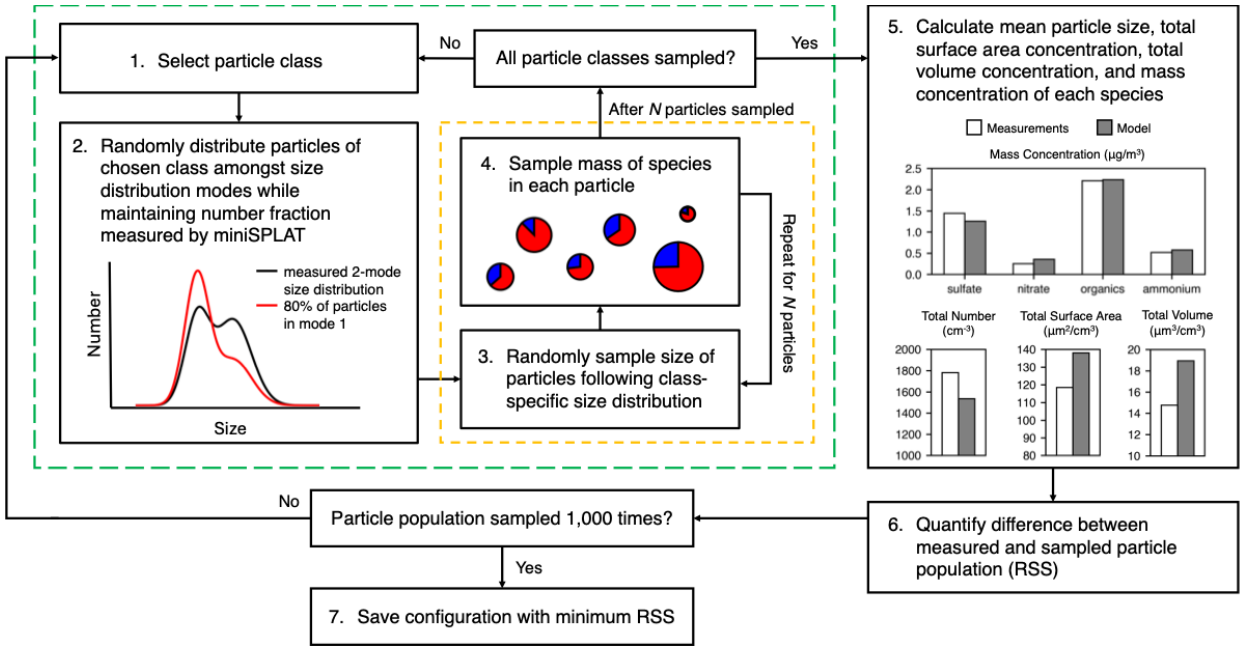

Figure S15. Overview of model initialization procedure. The measured size distribution is firstly fit with an N-modal size distribution function. The particles in each class are then distributed randomly amongst the modes of the fitted size distribution while preserving the total number fraction measured by the miniSPLAT (steps 1 and 2). The size and composition of each particle is then sampled (steps 3 and 4), and the properties of the sampled particle population are compared to measurements (steps 5 and 6). This process is repeated 1,000 times and the particle population which most closely matches the measurements is taken as the initial particle population in simulations. It should be noted that this initialization procedure is performed for each air parcel, meaning that each simulation has a unique initial particle population.

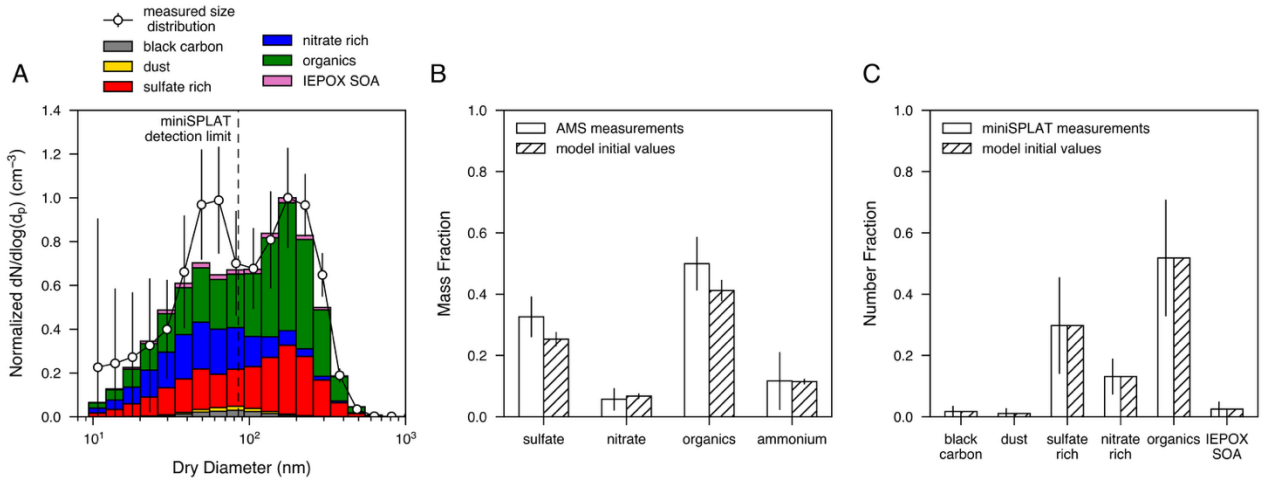

Figure S16. Initial size distribution, mass fraction of chemical species, and number fraction of particles assigned to each class. **(A)** Points show measured particle size distribution derived from a fast-integrating mobility spectrometer, passive cavity aerosol spectrometer probe, cloud and aerosol spectrometer, and fast cloud droplet probe. Bars show the average initial particle size distribution separated by particle class in simulations. The average initial mass fraction of chemical species in simulations agrees well with aerosol mass spectrometry measurements **(B)** and the average initial number fraction of particles in each class agrees well with miniSPLAT measurements **(C)**. The number fraction of particles in each class is calculated using only particles with diameter ≥ 85 nm (miniSPLAT 50% cut-off point). Error bars in each panel represent one standard deviation.